

OPTICS

Negative reflection of nanoscale-confined polaritons in a low-loss natural medium

Gonzalo Álvarez-Pérez^{1,2†}, Jiahua Duan^{1,2*†}, Javier Taboada-Gutiérrez^{1,2}, Qingdong Ou³, Elizaveta Nikulina⁴, Song Liu⁵, James H. Edgar⁵, Qiaoliang Bao^{3,6}, Vincenzo Giannini^{7,8,9}, Rainer Hillenbrand^{4,10}, Javier Martín-Sánchez^{1,2}, Alexey Yu Nikitin^{10,11*}, Pablo Alonso-González^{1,2*}

Negative reflection occurs when light is reflected toward the same side of the normal to the boundary from which it is incident. This exotic optical phenomenon is not only yet to be visualized in real space but also remains unexplored, both at the nanoscale and in natural media. Here, we directly visualize nanoscale-confined polaritons negatively reflecting on subwavelength mirrors fabricated in a low-loss van der Waals crystal. Our near-field nanoimaging results unveil an unconventional and broad tunability of both the polaritonic wavelength and direction of propagation upon negative reflection. On the basis of these findings, we introduce a device in nano-optics: a hyperbolic nanoresonator, in which hyperbolic polaritons with different momenta reflect back to a common point source, enhancing the intensity. These results pave way to realize nanophotonics in low-loss natural media, providing an efficient route to control nanolight, a key for future on-chip optical nanotechnologies.

INTRODUCTION

The control and manipulation of light and light-matter interactions at the nanoscale, the main aim of the field of nano-optics (1), is central to the development of next-generation nano-optical devices. In this regard, extensive efforts have been directed toward the understanding of fundamental optical phenomena at the nanoscale, such as reflection and refraction, even more so in their most exotic and counterintuitive versions: anomalous and negative reflection and refraction. For instance, planar lenses have been developed on the basis of anomalous refraction, and nanolight has been proved to reflect anomalously in nanocones made of hexagonal boron nitride (hBN) (2) and to be edge steerable along counterintuitive directions in microslits made of molybdenum trioxide (3), enabling novel avenues in nanophotonics. By contrast, negative reflection, which may provide another path toward manipulating light-matter excitations at the nanoscale, remains explored to a lesser extent. To date, this exotic phenomenon has only been observed for free-space light reflecting off artificially engineered interfaces (metasurfaces) (4–8) and chiral mirrors (9). A key disadvantage of these platforms is that they preclude the direct, real-space visualization of the phenomenon, which has been exceptionally difficult to accomplish experimentally, as not only low optical losses are required to guarantee a clear real-space visualization but also an adequate material platform. This real-space

visualization can provide crucial insights into a comprehensive understanding of such a fundamental optical phenomenon as reflection, opening so far the unexplored possibilities in nano-optics.

The recent findings of hyperbolic phonon polaritons (HPhPs) in low-dimensional van der Waals (vdW) crystals (10–18) have provided low-loss natural media to explore exotic optical phenomena at the nanoscale (19–29). In particular, HPhPs in α -MoO₃ are ideal candidates for these optical studies, since they guarantee a direct experimental visualization along the surface due to their in-plane hyperbolic dispersion, as recently demonstrated in planar refraction and focusing studies (27–30). Here, we demonstrate real-space visualization of negative reflection of polaritons at the nanoscale and in a low-loss vdW crystal (α -MoO₃), unveiling a nonintuitive, unconventional, and broad tunability of the polaritonic wavelength and direction of propagation, providing fundamental insights into reflection of nanolight. To do this, we introduce an optical scheme that combines near-field interferometry measurements of HPhPs in α -MoO₃ [using scattering-type near-field optical microscopy (s-SNOM); see Materials and Methods] with the design and fabrication of tilted edges with subwavelength dimensions acting as mirrors.

RESULTS

Our finding relies on the exotic properties of HPhPs, which stem from the anisotropic crystal structure of the host medium, giving rise to different optical responses along different crystal directions (31). The anisotropy of HPhPs is captured by their hyperbolic isofrequency curve (IFC; Fig. 1A), a slice of the dispersion surface in wave vector–frequency ($\mathbf{k}\omega$) space—where $\mathbf{k} = (k_x, k_y)$ is the polaritonic in-plane wave vector—by a plane of a constant frequency ω . The Poynting vector \mathbf{S} , which determines the direction of the polaritonic energy flux, and thus its propagation direction, is normal to the IFC. Hence, \mathbf{k} and \mathbf{S} are generally noncollinear in hyperbolic media, which has marked consequences in reflection phenomena. Specifically, upon momentum conservation at the boundary (the projection of the incident and reflected wave vectors on the boundary, k_{\parallel}^i , must be conserved, i.e., $\Delta k_{\parallel} = k_{\parallel}^r - k_{\parallel}^i = 0$), HPhPs can reflect at angles that are different to that of incidence,

¹Department of Physics, University of Oviedo, Oviedo 33006, Spain. ²Center of Research on Nanomaterials and Nanotechnology CINN (CSIC-Universidad de Oviedo), El Entrego 33940, Spain. ³Department of Materials Science and Engineering and ARC Centre of Excellence in Future Low-Energy Electronics Technologies (FLEET), Monash University, Clayton, Victoria, Australia. ⁴CIC nanoGUNE BRTA and Department of Electricity and Electronics, UPV/EHU, Donostia-San Sebastián 20018, Spain. ⁵Tim Taylor Department of Chemical Engineering, Kansas State University, Manhattan, KS 66506, USA. ⁶Nanjing kLight Laser Technology Co. Ltd., Nanjing 210032, China. ⁷Instituto de Estructura de la Materia (IEM), Consejo Superior de Investigaciones Científicas (CSIC), Serrano 121, Madrid 28006, Spain. ⁸Technology Innovation Institute, Building B04C, Abu Dhabi P.O. Box 9639, United Arab Emirates. ⁹Centre of Excellence, ENSEMBLE 3 Sp. z o.o., Wólczyńska 133, Warsaw 01-919, Poland. ¹⁰Ikerbasque, Basque Foundation for Science, Bilbao 48013, Spain. ¹¹Donostia International Physics Center (DIPC), Donostia-San Sebastián 20018, Spain. *Corresponding author. Email: pabloalonso@uniovi.es (P.A.-G.); alexey@dipc.org (A.Y.N.); duanjiahua@uniovi.es (J.D.)

†These authors contributed equally to this work.

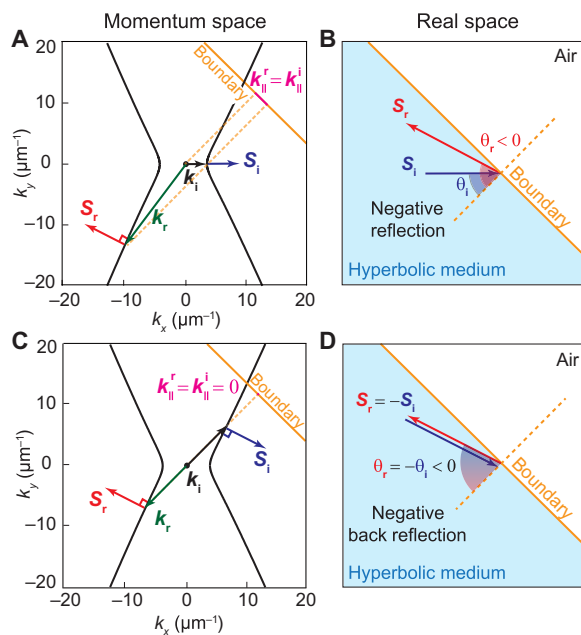


Fig. 1. Schematics of negative reflection of HPhPs. (A) Negative reflection of HPhPs upon momentum conservation at the boundary ($\Delta k_{\parallel} = k_{\parallel}^r - k_{\parallel}^i = 0$). The black solid line represents the IFC of HPhPs. \mathbf{k}_i and \mathbf{S}_i , generally noncollinear, indicate the wavefronts and Poynting vectors of the incident/reflected HPhPs, respectively. (B) Real-space illustration of negative reflection of HPhPs. The angle of reflection θ_r is negative, and \mathbf{S}_i and \mathbf{S}_r are on the same side of the normal to the boundary. (C) Negative back-reflection of HPhPs ($k_{\parallel}^r = k_{\parallel}^i = 0$), yielding $\mathbf{k}_i = -\mathbf{k}_r$, noncollinear with $\mathbf{S}_i = -\mathbf{S}_r$. (D) Real-space illustration of negative back-reflection of HPhPs, yielding only a single beam off the normal.

and the angle of reflection (θ_r ; calculated as the angle that the reflected energy flux \mathbf{S} forms with the normal to the boundary) can be even negative, i.e., \mathbf{S}_i and \mathbf{S}_r can be on the same side of the normal to the boundary (Fig. 1B). This is in stark contrast with the behavior in isotropic media, where the angle of reflection is positive and equal to that of incidence $\theta_r = \theta_i$ (specular reflection). In addition, the wave vector of the outgoing wave, k_r , can be much greater in modulus than that of incidence k_i , implying that the reflected wave can exhibit a much smaller wavelength, thereby providing a means to squeeze nanolight well beyond the diffraction limit by reflection. The phenomenon of negative reflection can be clearly pictured under the condition of back reflection. When the incident and reflected wave vectors are both normal to the reflecting boundary, i.e., $k_{\parallel}^r = k_{\parallel}^i = 0$ (Fig. 1C), the energy is reflected back to the source, i.e., $\mathbf{S}_r = -\mathbf{S}_i$ and $\theta_r = -\theta_i < 0$ (Fig. 1D). Hence, the incident and reflected beams propagate along the same direction, thereby interfering and giving rise to a neat picture of negative reflection, with only a single interference beam off the normal.

Crucially, back reflection is the optical scheme used in s-SNOM polariton interferometry (Materials and Methods) (32, 33), where near-field images are obtained by raster scanning a metallic tip that acts both as source and detector of polaritonic fields (Fig. 2A). Therefore, to experimentally demonstrate negative reflection at the nanoscale and in a natural medium, we performed s-SNOM polariton interferometry in α -MoO₃, which supports nanoscale-confined, low-loss in-plane HPhPs in the mid-infrared range (34). Specifically, we study HPhPs back-reflecting at edges fabricated in thin slabs of

α -MoO₃ by focused ion beam (Materials and Methods). By carefully selecting the angle φ that the edges form with respect to the [100] crystal axis of α -MoO₃ and by fabricating them with subwavelength dimensions, we can unambiguously probe negative back reflection of HPhPs along specific directions, avoiding the interference with HPhPs propagating along other directions (the use of large edges acting as mirrors would hinder the identification of the reflection direction due to interference effects; see fig. S4). In addition, the subwavelength edges are slightly rounded at their terminations to avoid the strong launching of HPhPs, which would also produce interferences that would distort our real-space visualization of negative reflection.

As a representative example, we fabricate edges tilted at an angle $\varphi = 38^\circ$, thereby probing polaritonic states close to the asymptote of the hyperbolic IFC, where the noncollinearity between \mathbf{k} and \mathbf{S} is maximal (fig. 2A). By s-SNOM imaging, we observe interferometric fringes revealing that HPhPs anomalously back-reflect at counter-intuitive directions (Fig. 2B). In particular, the Poynting vector of the back-reflected wave (indicated by the direction of the maxima of the near-field amplitude) (3, 10) is along the same side of the normal to the boundary as the incident one, unambiguously demonstrating negative reflection of HPhPs at an angle $\theta_r = -76^\circ$. In addition, the back-reflected wave fronts appear tilted with respect to the direction of propagation and almost parallel to it (see sections S1 and S2), which is explained by \mathbf{k} and \mathbf{S} being almost perpendicular at some points of the hyperbolic IFC (Fig. 2A). To corroborate our experimental images and whether they demonstrate the negative reflection of PhPs, we perform full-wave simulations mimicking the experiment (see Materials and Methods). Figure 2C represents the absolute value of the z component of the electric field distribution, $|E_z|$, created by a vertical point dipole (representing the experimental tip; see Materials and Methods) at a fixed lateral position (chosen along the expected direction of negatively reflected PhPs according to Fig. 2A). We can clearly recognize similar tilted interference fringes as those observed in the near-field image, thus unambiguously demonstrating the back reflection of PhPs at the mirror. For comparison, we also visualize in-plane isotropic polaritons back-reflecting on mirrors fabricated in isotopically enriched h¹⁰BN (Fig. 2D) (17). As expected, we observe interference fringes parallel to all the mirrors (Fig. 2E) and thus along all in-plane directions, in excellent agreement with our simulations (Fig. 2F).

To gain further insights into the negative reflection at the nanoscale, we study the dependence of the polaritonic wavelength λ_p and the angle of reflection θ_r as a function of the angle of the mirror φ and incident frequency ω_0 . To do so, we fabricate mirrors in α -MoO₃ at different angles of $\varphi = 38^\circ$, 60° , and 90° and perform s-SNOM polariton interferometry of back-reflected HPhPs. Since, in anisotropic media, the wave vector is direction dependent, λ_p changes depending on the direction along which we map back reflection and hence on φ . By selecting φ , we probe the behavior of HPhPs upon negative reflection for different \mathbf{k} and \mathbf{S} , i.e., different angles of incidence. This is illustrated in Fig. 3 (A and B) for $\omega_0 = 889 \text{ cm}^{-1}$.

Clearly, λ_p and θ_r change as a function of φ . Specifically, as a result of the hyperbolic-like shape of the IFC, when φ decreases (from 90° to 20°), k_i and k_r approach the asymptote (see black and cyan arrows in Fig. 3, A to C), and λ_p can be markedly squeezed (from 2.5 to 0 μm ; Fig. 3D, top), while, on the other hand, θ_r takes values in a very broad angular sector (from 0° to -80° ; Fig. 3D,

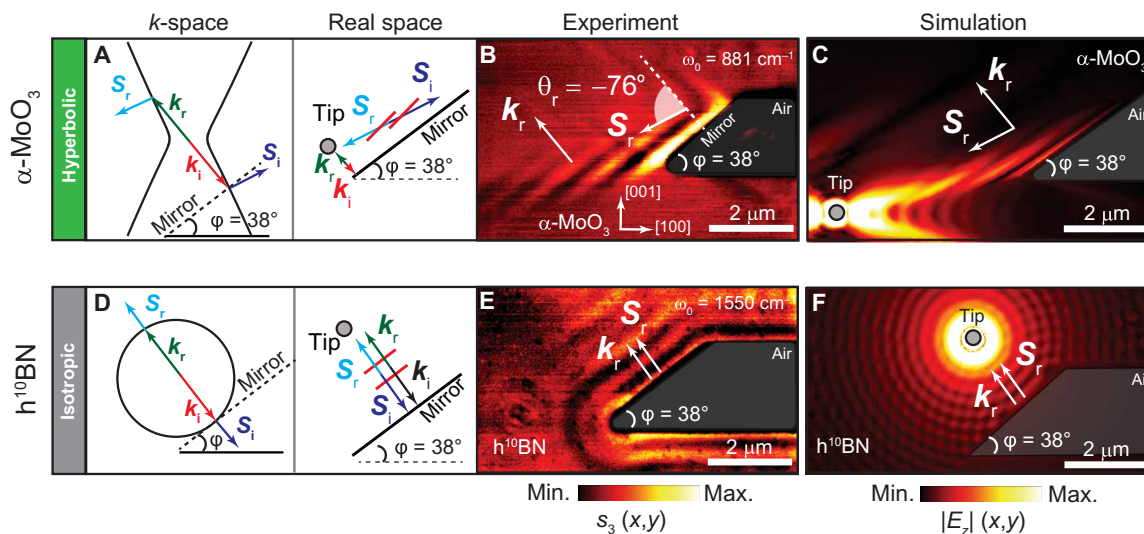


Fig. 2. Visualization of negative reflection of nanoscale-confined polaritons in a natural medium. Illustration of back-reflection of HPhPs in k -space and real space for (A) in-plane hyperbolic and (D) in-plane isotropic media. (B and E) Experimental s -SNOM amplitude image $s_3(x, y)$ of HPhPs back-reflecting on mirrors tilted at an angle of $\varphi = 38^\circ$ fabricated on α -MoO₃ and h¹⁰BN, respectively. $k_{i,r}$ and $S_{i,r}$ indicate the wavefronts and Poynting vectors of the incident/reflected HPhPs, respectively. (C and F) Full-wave numerical simulation $E_z(x, y)$ of back-reflected polaritons excited by a point dipole on α -MoO₃ and h¹⁰BN, respectively.

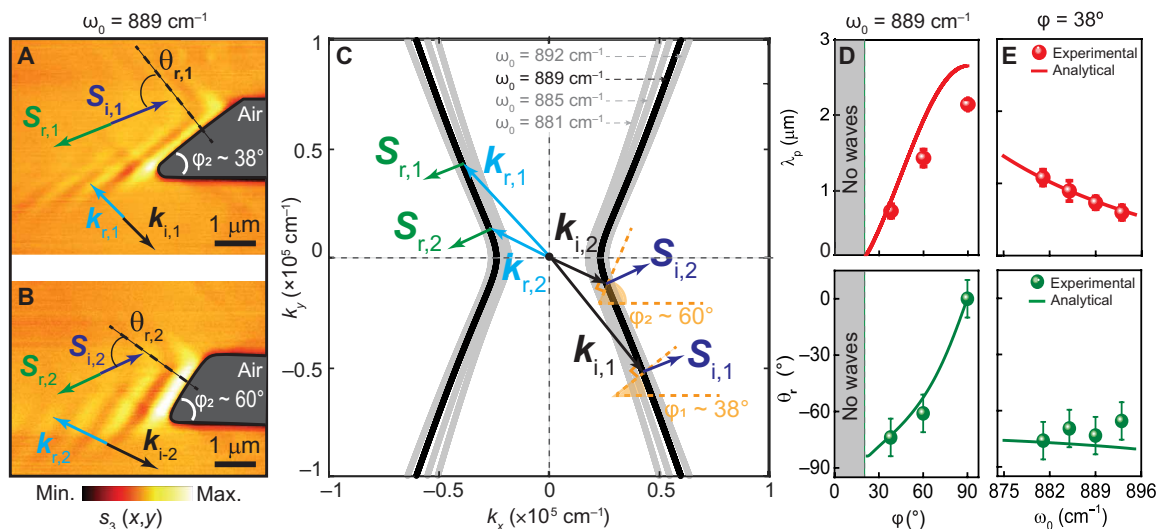


Fig. 3. Properties of negative reflection of HPhPs in α -MoO₃. (A and B) Experimental near-field images $s_3(x, y)$ of HPhPs back-reflecting on mirrors fabricated in α -MoO₃ tilted at $\varphi = 38^\circ$ and 60° , respectively. The incident frequency is $\omega_0 = 889 \text{ cm}^{-1}$. (C) IFC of HPhPs showing the directions of $k_{i,r}$ and $S_{i,r}$ of the incident and back-reflected HPhPs on mirrors tilted at $\varphi = 38^\circ$ and 60° at $\omega_0 = 889$ (black line), 892, 885, and 881 cm^{-1} (gray lines). (D and E) Dependence of the polaritonic wavelength λ_p (top) and angle of reflection θ_r (bottom) on φ ($\omega_0 = 889 \text{ cm}^{-1}$) and ω_0 ($\varphi = 38^\circ$), respectively. The continuous lines in (D) and (E) are extracted from analytical calculations and the symbols from experimental s -SNOM images.

bottom). Note that φ values smaller than 20° are forbidden, since the corresponding wave vectors are not allowed by the hyperbolic IFC (gray shaded area). The continuous lines show calculations based on the analytical IFC and momentum conservation at the mirror, in excellent agreement with the experiment. Note that the reasonable deviation in the top panel of Fig. 3D may be caused by the focused ion beam process involved in the fabrication of the reflectors, which may induce a gradient thickness in the α -MoO₃ slab. Together, these results show that both λ_p and θ_r exhibit an unconventional and broad tunability as a function of φ , in stark

contrast to back-reflected polaritons in isotropic media, where the same λ_p and θ_r is obtained for all φ . We note that polariton interferometry of back-reflected polaritons is the technique that allows us to probe these exotic aspects of negative reflection, yet the conclusions are broader and apply beyond the case of back reflection and even of negative reflection, providing a strategy to squeeze and steer nanolight.

Given the strong dispersive nature of the back-reflected polaritons, we further study their dependence upon ω_0 . The top and bottom panels in Fig. 3E represent λ_p and θ_r as a function of ω_0 , respectively,

together with analytical calculations (green continuous lines), showing an excellent agreement. The spectral dependence demonstrates that λ_p and θ_r can be tuned between 0.6 and 1.1 μm and -76° and -65° , respectively, when ω_0 varies from 881 to 893 cm^{-1} . Note that this dependence does not hold in isotropic media, where θ_r is always equal to zero under back reflection regardless of ω_0 .

Following our findings and basic understanding on negative back reflection, we further derive the analytical shape of a polaritonic mirror capable of reflecting all the incident HPhPs back to their source, i.e., a hyperbolic retroreflector. This curve must be such that every incident wave vector is perpendicular to it. In isotropic media, this condition is satisfied by a circumference (inset in Fig. 4A). However, in hyperbolic media, because of the noncollinearity of \mathbf{k} and \mathbf{S} , the condition yields the following hyperbola (section S6)

$$y(x) = \pm \sqrt{\frac{x^2 |\epsilon_y|}{|\epsilon_x|} - a^2} \quad (1)$$

where x and y are the directions along the main and conjugate axes of the hyperbola, ϵ_x and ϵ_y are the dielectric permittivities along x and y , and a is the distance between the center and the vertex of the hyperbola (see the Supplementary Materials). Figure 4A shows numerical simulations of the electric field $\text{Re}[E_z(x, y)]$ on a $\alpha\text{-MoO}_3$ slab using a retroreflector whose shape is given in Eq. 1 for HPhPs in $\alpha\text{-MoO}_3$ at an incident frequency of $\omega_0 = 920 \text{ cm}^{-1}$ and a distance a equal to $\lambda_p = 1.7 \mu\text{m}$, where λ_p is the analytical polariton wavelength along the x direction ([100] crystal direction) (35). Polaritons are launched by a point dipole to study just the reflection phenomena. Focusing of hyperbolic polaritons with far-field illumination beams has been studied in prior works (see also section S7) (28–30). All the incident waves reflect to the location of the source, yielding a

standing wave pattern (see the Supplementary Materials) and an enhancement of the intensity at the source of approximately +35%. Figure 4B shows a comparison with a standard reflector, such as a straight edge, in which HPhPs propagate far away from the source (red arrows in Fig. 4B). By mirroring the hyperbolic retroreflector structure with respect to the location of the source, we design an optical nanoresonator for in-plane HPhPs (Fig. 4C), in which all the hyperbolic waves launched by a dipole located at its center continuously reflect back between its boundaries (the absolute value of the field is shown in the Supplementary Materials). In this case, the intensity at the source is enhanced approximately +64%. We note that this value is very robust to displacements of the dipole of up to 1 μm inside the cavity, both along the x and y directions, which is vital for practical purposes. While this value could be further improved by making the cavity dimensions smaller, here, we introduce a first proof-of-concept hyperbolic nanoresonator that exploits both the strong directionality of in-plane HPhPs and their high momenta to enhance light-matter interactions and hence with outstanding prospects for nanophotonics (36).

DISCUSSION

In conclusion, we have demonstrated the negative reflection of nanoscale-confined HPhPs in a low-loss natural medium ($\alpha\text{-MoO}_3$). Our study unveils an unconventional tunability of the direction of propagation and wavelength of the negatively reflected HPhPs as a function of the incident frequency ω_0 and the angle of the mirror φ , opening a plethora of possibilities to control nanolight by reflection in hyperbolic media. These fundamental insights allowed us to develop an optical nanodevice: a hyperbolic nanoresonator. Because of the high density of optical states in hyperbolic media, these cavities hold promises for controlling the decay rates of emitters.

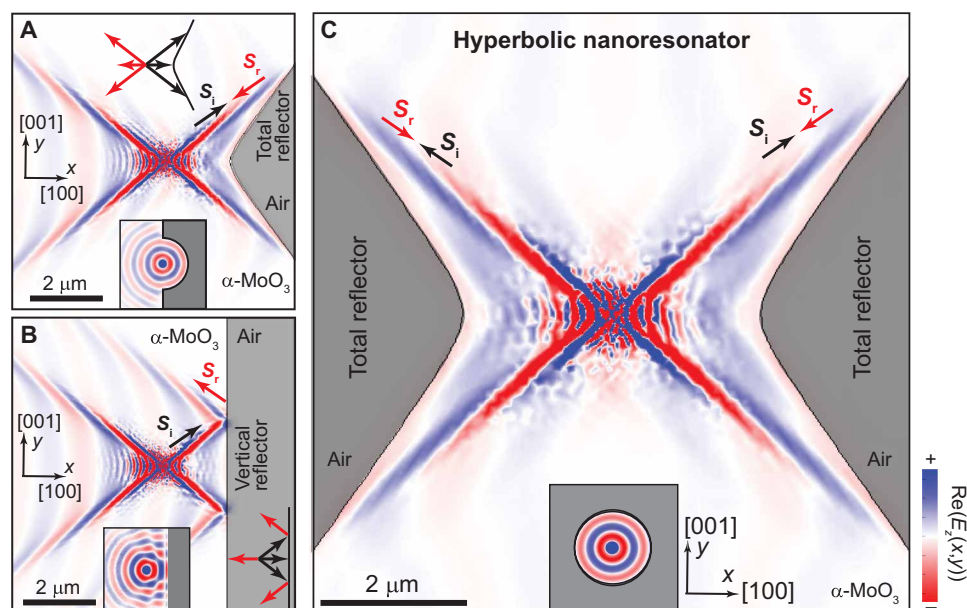


Fig. 4. Retroreflector and nanoresonator for HPhPs. Simulated near-field image $\text{Re}[E_z(x, y)]$ of HPhPs reflecting on (A) a hyperbolic retroreflector, (B) a straight edge, and (C) a hyperbolic nanoresonator consisting of two retroreflectors on a 200-nm-thick $\alpha\text{-MoO}_3$ slab at an incident laser frequency of $\omega_0 = 920 \text{ cm}^{-1}$. The source is a point dipole located at a distance equal to the HPhP wavelength of $\lambda_p = 1.7 \mu\text{m}$ from the edge. The insets show $\text{Re}[E_z(x, y)]$ of isotropic polaritons upon reflection on (A) a retroreflector in isotropic media (a semi-circumference), (B) a straight edge, and (C) a nanoresonator in isotropic media (a circumference).

In addition, open cavities as our hyperbolic nanoresonator are more accessible from the outside and thus experimentally preferred to design a photonic circuit. Together, our findings provide a route for controlling and manipulating the flow of energy at the nanoscale by using hyperbolic waves and for squeezing light to nano- or sub-wavelength scales, thereby enabling to compress and enhance light-matter interactions to unprecedentedly small volumes, the general premise of nanophotonics. Our results thus hold promises for the development of applications in optoelectronics, biosensing, nano-imaging, and chemistry.

MATERIALS AND METHODS

Sample fabrication

High-quality α -MoO₃ flakes on the SiO₂ (300 nm)/Si substrate were prepared via mechanical exfoliation of bulk crystals. The sub-wavelength mirrors in α -MoO₃ were then fabricated by focused ion beam etching, followed by a thermal annealing process; see (3, 20) here.

Selected hBN flakes on Si/SiO₂ substrates were milled into a desired shape by using focused Ga-ion beam in a FEI Helios 450S Dual Beam System. The structures were fabricated under the following Ga-ion beam conditions: accelerating voltage of 30 kV, beam current of 33 pA, and dose of 333.54 pc/ μ m². To minimize an ion beam damage of the hBN flakes, solely the contours of the structures were milled away.

The thicknesses of the α -MoO₃ flakes shown in Figs. 2 and 3 here is 250 nm. The thickness of the h¹⁰BN flake shown in Fig. 2 is 120 nm.

Scattering-type scanning near-field optical microscopy

Infrared nanoimaging was performed using a commercially available s-SNOM from Neaspec, where a metallized (Pt-coated) cantilevered atomic force microscope tip is used as a scattering near-field probe. The tip oscillates vertically at the mechanical resonant frequency (around 270 kHz) of the cantilever, with an amplitude of about 50 nm. The sample is illuminated with infrared light at frequency ω_0 (from tunable CO₂ and quantum cascade lasers). The nanoscale hotspot at the tip apex acts as a local source of polaritons, which are recorded by the same tip upon back reflection, i.e., the tip-launched polaritons reflect at the flake edges and return to the tip, meeting the condition $k_{\parallel}^r = k_{\parallel}^i = 0$ ($\mathbf{S}_r = -\mathbf{S}_i$), producing polariton interference, and yielding fringes in the near-field images separated by half the polariton wavelength along the studied direction (polariton interferometry). The tip-scattered field is recorded with a pseudo-heterodyne Michelson interferometer. Demodulation of the interferometric detector signal at the n^{th} harmonics of the tip oscillation frequency yields the complex-valued near-field signals $\sigma_n = s_n e^{i\phi_n}$, with s_n being the near-field amplitude and ϕ_n being the near-field phase. By recording the near-field signals as a function of the lateral tip position, we obtain near-field images.

The error bars in Fig. 3 are obtained as follows: In λ_p , they are the result of averaging five line profiles in the near-field images, while for θ_p , we take a conservative error of $\pm 10^\circ$.

Analytical calculations of the IFC

To theoretically analyze the angle of reflection and the angle between the wave vector and the Poynting vector, we use the dispersion relation of polaritons in a biaxial slab embedded between two semi-infinite isotropic media (35)

$$k(\omega) = \frac{\rho}{d} \left[\arctan\left(\frac{\epsilon_1 \rho}{\epsilon_z}\right) + \arctan\left(\frac{\epsilon_3 \rho}{\epsilon_z}\right) + \pi l \right], \quad l = 0, 1, 2, \dots$$

where d is the thickness of the biaxial slab, k is the in-plane momentum ($k^2 = k_x^2 + k_y^2$), α is the angle between the x axis and k , $\rho = i \sqrt{\frac{\epsilon_z}{\epsilon_x \cos^2 \alpha + \epsilon_y \sin^2 \alpha}}$, and l is the mode index. Solving this dispersion relation for α between 0° and 360° , we calculate the IFC for HPhPs in slabs of α -MoO₃ on top of SiO₂ (with the air as superstrate) at several incident frequencies.

Full-wave numerical simulations

In s-SNOM experiments, the tip acts as an optical antenna converting the incident light into a strongly confined near field below the tip apex, providing the necessary momentum to excite PhPs. However, because of the complex near-field interaction between the tip and the sample, numerical quantitative studies of s-SNOM experiments meet substantial difficulties in simulating near-field images (37). To overcome these difficulties, we approximate the tip by a dipole source (with a constant dipole moment) (38), in contrast to the usual dipole model, in which the effective dipole moment is given by the product of the exciting electric field and the polarizability of a sphere (39). We assume that the polarizability of the dipole is weakly affected by the PhPs excited in the polaritonic slabs (see Fig. 2), and their back action onto the tip can be thus neglected. Calculating the amplitude of the near field, $|E_z|$, we simulate near-field images (we use COMSOL Multiphysics). The experimental s-SNOM images agree well with our simulated images, which lets us conclude that the calculated field between the dipole and the slabs, E_z , provides a valid numerical description of the signals measured by s-SNOM.

The thicknesses of the α -MoO₃ flakes shown in Figs. 2 and 3 here is 250 nm. The thickness of the h¹⁰BN flake shown in Fig. 2 is 120 nm. The thickness of the α -MoO₃ flakes shown in Fig. 4 is 200 nm.

Intensity enhancement under the dipole source

The intensity enhancement ΔI_z produced by the total hyperbolic reflector is calculated as $\Delta I_z = (\Delta E_z)^2$, where ΔE_z is the electric field enhancement

$$\Delta E_z = \frac{E_z^R}{E_z^0} - 1$$

with E_z^R and E_z^0 as the z components of the electric field created by a dipole source placed on top of the system, with and without reflector, respectively. Both E_z^R and E_z^0 are probed at the location of the source, thereby providing a simple means to cancel the contribution from the dipole to the field enhancement. Pulling out the enhancement factor with further confidence with the strong dipole source is nontrivial and falls beyond the scope of this work.

SUPPLEMENTARY MATERIALS

Supplementary material for this article is available at <https://science.org/doi/10.1126/sciadv.abp8486>

REFERENCES AND NOTES

1. L. Novotny, B. Hecht, *Principles of Nano-Optics* (Cambridge Univ. Press, 2012).
2. A. J. Giles, S. Dai, O. J. Glembocki, A. V. Kretinin, Z. Sun, C. T. Ellis, J. G. Tischler, T. Taniguchi, K. Watanabe, M. M. Fogler, K. S. Novoselov, D. N. Basov, J. D. Caldwell, Imaging of anomalous internal reflections of hyperbolic phonon-polaritons in hexagonal boron nitride. *Nano Lett.* **16**, 3858–3865 (2016).

3. Z. Dai, G. Hu, G. Si, Q. Ou, Q. Zhang, S. Balendhran, F. Rahman, B. Y. Zhang, J. Z. Ou, G. Li, A. Alù, C.-W. Qiu, Q. Bao, Edge-oriented and steerable hyperbolic polaritons in anisotropic van der Waals nanocavities. *Nat. Commun.* **11**, 6086 (2020).
4. N. Yu, P. Genevet, M. A. Kats, F. Aieta, J. P. Tetienne, F. Capasso, Z. Gaburro, Light propagation with phase discontinuities: Generalized laws of reflection and refraction. *Science* **334**, 333–337 (2011).
5. F. Aieta, P. Genevet, N. Yu, M. A. Kats, Z. Gaburro, F. Capasso, Out-of-plane reflection and refraction of light by anisotropic optical antenna metasurfaces with phase discontinuities. *Nano Lett.* **12**, 1702–1706 (2012).
6. B. Liu, W. Zhao, Y. Jiang, Apparent negative reflection with the gradient acoustic metasurface by integrating supercell periodicity into the generalized law of reflection. *Sci. Rep.* **6**, 38314 (2016).
7. S. Liu, T. J. Cui, A. Noor, Z. Tao, H. C. Zhang, G.-D. Bai, Y. Yang, X. Y. Zhou, Negative reflection and negative surface wave conversion from obliquely incident electromagnetic waves. *Light: Sci. Appl.* **7**, 18008 (2018).
8. B. Gérardin, J. Laurent, F. Legrand, C. Prada, A. Aubry, Negative reflection of elastic guided waves in chaotic and random scattering media. *Sci. Rep.* **9**, 2135 (2019).
9. C. Zhang, Negative reflections of electromagnetic waves in a strong chiral medium. *Appl. Phys. Lett.* **91**, 194101 (2007).
10. T. Low, A. Chaves, J. D. Caldwell, A. Kumar, N. X. Fang, P. Avouris, T. F. Heinz, F. Guinea, L. Martin-Moreno, F. Koppens, Polaritons in layered two-dimensional materials. *Nat. Mater.* **16**, 182–194 (2017).
11. D. N. Basov, M. M. Fogler, F. J. García de Abajo, Polaritons in van der Waals materials. *Science* **354**, aag1992 (2016).
12. S. Dai, Z. Fei, Q. Ma, A. S. Rodin, M. Wagner, A. S. McLeod, M. K. Liu, W. Gannett, W. Regan, K. Watanabe, T. Taniguchi, M. Thiemens, G. Dominguez, A. H. C. Neto, A. Zettl, F. Keilmann, P. Jarillo-Herrero, M. M. Fogler, D. N. Basov, Tunable phonon polaritons in atomically thin van der Waals crystals of boron nitride. *Science* **343**, 1125–1129 (2014).
13. J. D. Caldwell, A. V. Kretinin, Y. Chen, V. Giannini, M. M. Fogler, Y. Francescato, C. T. Ellis, J. G. Tischler, C. R. Woods, A. J. Giles, M. Hong, K. Watanabe, T. Taniguchi, S. A. Maier, K. S. Novoselov, Sub-diffractive volume-confined polaritons in the natural hyperbolic material hexagonal boron nitride. *Nat. Commun.* **5**, 5221 (2014).
14. A. J. Giles, S. Dai, I. Vurgaftman, T. Hoffman, S. Liu, L. Lindsay, C. T. Ellis, N. Assefa, I. Chatzakos, T. L. Reinecke, J. G. Tischler, M. M. Fogler, J. H. Edgar, D. N. Basov, J. D. Caldwell, Ultralow-loss polaritons in isotopically pure boron nitride. *Nat. Mater.* **17**, 134–139 (2018).
15. J. D. Caldwell, I. Aharonovich, G. Cassabois, J. H. Edgar, B. Gil, D. N. Basov, Photonics with hexagonal boron nitride. *Nat. Rev. Mater.* **4**, 552–567 (2019).
16. W. Ma, P. Alonso-González, S. Li, A. Y. Nikitin, J. Yuan, J. Martín-Sánchez, J. Taboada-Gutiérrez, I. Amenabar, P. Li, S. Vélez, C. Tollan, Z. Dai, Y. Zhang, S. Sriram, K. Kalantar-Zadeh, S.-T. Lee, R. Hillenbrand, Q. Bao, In-plane anisotropic and ultra-low-loss polaritons in a natural van der Waals crystal. *Nature* **562**, 557–562 (2018).
17. Z. Zheng, N. Xu, S. L. Oscurato, M. Tamagnone, F. Sun, Y. Jiang, Y. Ke, J. Chen, W. Huang, W. L. Wilson, A. Ambrosio, S. Deng, H. Chen, A mid-infrared biaxial hyperbolic van der Waals crystal. *Sci. Adv.* **5**, eaav8690 (2019).
18. J. Taboada-Gutiérrez, G. Álvarez-Pérez, J. Duan, W. Ma, K. Crowley, I. Prieto, A. Bylinkin, M. Autore, H. Volkova, K. Kimura, T. Kimura, M.-H. Berger, S. Li, Q. Bao, X. P. A. Gao, I. Errea, A. Y. Nikitin, R. Hillenbrand, J. Martín-Sánchez, P. Alonso-González, Broad spectral tuning of ultra-low-loss polaritons in a van der Waals crystal by intercalation. *Nat. Mater.* **19**, 964–968 (2020).
19. J. Duan, N. Capote-Robayna, J. Taboada-Gutiérrez, G. Álvarez-Pérez, I. Prieto, J. Martín-Sánchez, A. Y. Nikitin, P. Alonso-González, Twisted nano-optics: Manipulating light at the nanoscale with twisted phonon polaritonic slabs. *Nano Lett.* **20**, 5323–5329 (2020).
20. G. Hu, Q. Ou, G. Si, Y. Wu, J. Wu, Z. Dai, A. Krasnok, Y. Mazor, Q. Zhang, Q. Bao, C.-W. Qiu, A. Alù, Topological polaritons and photonic magic angles in twisted α -MoO₃ bilayers. *Nature* **582**, 209–213 (2020).
21. M. Chen, X. Lin, T. H. Dinh, Z. Zheng, J. Shen, Q. Ma, H. Chen, P. Jarillo-Herrero, S. Dai, Configurable phonon polaritons in twisted α -MoO₃. *Nat. Mater.* **19**, 1307–1311 (2020).
22. Z. Zheng, F. Sun, W. Huang, J. Jiang, R. Zhan, Y. Ke, H. Chen, S. Deng, Phonon polaritons in twisted double-layers of hyperbolic van der Waals crystals. *Nano Lett.* **20**, 5301–5308 (2020).
23. P. Li, G. Hu, I. Dolado, M. Tymchenko, C.-W. Qiu, F. J. Alfaro-Mozaz, F. Casanova, L. E. Hueso, S. Liu, J. H. Edgar, S. Vélez, A. Alu, R. Hillenbrand, Collective near-field coupling and nonlocal phenomena in infrared-phononic metasurfaces for nano-light canalization. *Nat. Commun.* **11**, 3663 (2020).
24. I.-H. Lee, M. He, X. Zhang, Y. Luo, S. Liu, J. H. Edgar, K. Wang, P. Avouris, T. Low, J. D. Caldwell, S.-H. Oh, Image polaritons in boron nitride for extreme polariton confinement with low losses. *Nat. Commun.* **11**, 3649 (2020).
25. S. Dai, Q. Ma, T. Andersen, A. S. McLeod, Z. Fei, M. K. Liu, M. Wagner, K. Watanabe, T. Taniguchi, M. Thiemens, F. Keilmann, P. Jarillo-Herrero, M. M. Fogler, D. N. Basov, Subdiffractive focusing and guiding of polaritonic rays in a natural hyperbolic material. *Nat. Commun.* **6**, 6963 (2015).
26. P. Li, M. Lewin, A. V. Kretinin, J. D. Caldwell, K. S. Novoselov, T. Taniguchi, K. Watanabe, F. Gaussmann, T. Taubner, Hyperbolic phonon-polaritons in boron nitride for near-field optical imaging and focusing. *Nat. Commun.* **6**, 7507 (2015).
27. J. Duan, G. Álvarez-Pérez, A. I. F. Tresguerres-Mata, J. Taboada-Gutiérrez, K. V. Voronin, A. Bylinkin, B. Chang, S. Xiao, S. Liu, J. H. Edgar, J. I. Martín, V. S. Volkov, R. Hillenbrand, J. Martín-Sánchez, A. Y. Nikitin, P. Alonso-González, Planar refraction and lensing of highly confined polaritons in anisotropic media. *Nat. Commun.* **12**, 4325 (2021).
28. J. Martín-Sánchez, J. Duan, J. Taboada-Gutiérrez, G. Álvarez-Pérez, K. V. Voronin, I. Prieto, W. Ma, Q. Bao, V. S. Volkov, R. Hillenbrand, A. Y. Nikitin, P. Alonso-González, Focusing of in-plane hyperbolic polaritons in van der Waals crystals with tailored infrared nanoantennas. *Sci. Adv.* **7**, eabj0127 (2021).
29. Z. Zheng, J. Jiang, N. Xu, X. Wang, W. Huang, Y. Ke, S. Zhang, H. Chen, S. Deng, Controlling and focusing in-plane hyperbolic phonon polaritons in α -MoO₃ with a curved plasmonic antenna. *Adv. Mater.* **34**, 2104164 (2021).
30. Y. Qu, N. Chen, H. Teng, H. Hu, J. Sun, R. Yu, D. Hu, M. Xue, C. Li, B. Wu, J. Chen, Z. Sun, M. Liu, Y. Liu, F. Javier Garcia de Abajo, Q. Dai, Tunable planar focusing based on hyperbolic phonon polaritons in MoO₃. *Adv. Mater.* **34**, 2105590 (2022).
31. L. D. Landáu, E. M. Lifshits, *Electrodynamics of Continuous Media* (Pergamon Press, 1960).
32. J. Chen, M. Badioli, P. Alonso-González, S. Thongrattanasiri, F. Huth, J. Osmond, M. Spasenović, A. Centeno, A. Pesquera, P. Godignon, A. Zurutuza Elorza, N. Camara, F. J. García de Abajo, R. Hillenbrand, F. H. L. Koppens, Optical nano-imaging of gate-tunable graphene plasmons. *Nature* **487**, 77–81 (2012).
33. Z. Fei, A. S. Rodin, G. O. Andreev, W. Bao, A. S. McLeod, M. Wagner, L. M. Zhang, Z. Zhao, M. Thiemens, G. Dominguez, M. M. Fogler, A. H. Castro Neto, C. N. Lau, F. Keilmann, D. N. Basov, Gate-tuning of graphene plasmons revealed by infrared nano-imaging. *Nature* **487**, 82–85 (2012).
34. G. Álvarez-Pérez, T. G. Folland, I. Errea, J. Taboada-Gutiérrez, J. Duan, J. Martín-Sánchez, A. I. F. Tresguerres-Mata, J. R. Matson, A. Bylinkin, M. He, W. Ma, Q. Bao, J. I. Martín, J. D. Caldwell, A. Y. Nikitin, P. Alonso-González, Infrared permittivity of the biaxial van der Waals semiconductor α -MoO₃ from near- and far-field correlative studies. *Adv. Mater.* **32**, 1908176 (2020).
35. G. Álvarez-Pérez, K. V. Voronin, V. S. Volkov, P. Alonso-González, A. Y. Nikitin, Analytical approximations for the dispersion of electromagnetic modes in slabs of biaxial crystals. *Phys. Rev.* **100**, 235408 (2019).
36. H. H. Sheinfux, L. Orsini, M. Jung, I. Torre, M. Ceccanti, R. A. Maniyara, D. B. Ruiz, S. Castilla, N. C. H. Hesp, E. Janzen, V. Pruneri, J. H. Edgar, G. Shvets, Bound in the continuum modes in indirectly-patterned hyperbolic media. *Res. Square* 10.21203/rs.3.rs-385236/v1 (2021).
37. A. S. McLeod, P. Kelly, M. D. Goldflam, Z. Gainsforth, A. J. Westphal, G. Dominguez, M. H. Thiemens, M. M. Fogler, D. N. Basov, Model for quantitative tip-enhanced spectroscopy and the extraction of nanoscale-resolved optical constants. *Phys. Rev. B* **90**, 085136 (2014).
38. A. Y. Nikitin, P. Alonso-González, S. Vélez, S. Mastel, A. Centeno, A. Pesquera, A. Zurutuza, F. Casanova, L. E. Hueso, F. H. L. Koppens, R. Hillenbrand, Real-space mapping of tailored sheet and edge plasmons in graphene nanostructures. *Nat. Photonics* **10**, 239–243 (2016).
39. R. Hillenbrand, F. Keilmann, Complex optical constants on a subwavelength scale. *Phys. Rev. Lett.* **85**, 3029–3032 (2000).
40. P. Pons-Valencia, F. J. Alfaro-Mozaz, M. M. Wiecha, V. Bielek, I. Dolado, S. Vélez, P. Li, P. Alonso-González, F. Casanova, L. E. Hueso, L. Martín-Moreno, Launching of hyperbolic phonon-polaritons in h-BN slabs by resonant metal plasmonic antennas. *Nat. Commun.* **10**, 3242 (2019).
41. P. Alonso-González, A. Y. Nikitin, F. Golmar, A. Centeno, A. Pesquera, S. Vélez, J. Chen, G. Navickaite, F. Koppens, A. Zurutuza, F. Casanova, L. E. Hueso, R. Hillenbrand, Controlling graphene plasmons with resonant metal antennas and spatial conductivity patterns. *Science* **344**, 1369–1373 (2014).

Acknowledgments

Funding: G.Á.-P. and J.T.-G. acknowledge support through the Severo Ochoa Program from the Government of the Principality of Asturias (grant numbers PA-20-PF-BP19-053 and PA-18-PF-BP17-126, respectively). Q.O. acknowledges support from the Australian Research Council (ARC; CE170100039 and DE220100154). This work was performed in part at the Melbourne Centre for Nanofabrication (MCN) in the Victorian Node of the Australian National Fabrication Facility (ANFF). hBN crystal growth was supported by the National Science Foundation award number CMMI 1538127. V.G. acknowledges the Ministerio de Ciencia, Innovación y Universidades through the grant MELODIA (PGC2018-095777-B-C21). V.G. thanks the “ENSEMBLE 3—Centre of Excellence for nanophotonics, advanced materials and novel crystal growth-based technologies” project (GA no. MAB/2020/14) carried out within the International Research Agendas program of the Foundation for Polish Science cofinanced by the European Union under the European Regional Development Fund and the European Union’s Horizon 2020 research and innovation programme Teaming for Excellence (GA no.

857543) for support of this work. R.H. acknowledges financial support from the Spanish Ministry of Science, Innovation and Universities (national project RTI2018-094830-B-100 and the project MDM-2016-0618 of the María de Maeztu Units of Excellence Program) and the Basque Government (grant no. IT1164-19). J.M.-S. acknowledges financial support from the Ramón y Cajal Program of the Government of Spain and FSE (RYC2018-026196-I) and the Spanish Ministry of Science and Innovation (State Plan for Scientific and Technical Research and Innovation grant number PID2019-110308GA-I00). A.Y.N. acknowledges the Spanish Ministry of Science and Innovation (grants MAT201788358-C3-3-R and PID2020-115221GB-C42) and the Basque Department of Education (grant PIBA-2020-1-0014). P.A.-G. acknowledges support from the European Research Council under starting grant no. 715496, 2DNANOPTICA and the Spanish Ministry of Science and Innovation (State Plan for Scientific and Technical Research and Innovation grant number PID2019-111156GB-I00). Q.B. acknowledges the support from Shenzhen Nanshan District Pilotage Team Program (LHTD20170006). **Author contributions:** P.A.-G., G.Á.-P., and J.D. conceived the study. J.D. and J.T.-G. fabricated the samples and performed the near-field imaging experiments with assistance from J.M.-S. Q.O. and E.N. carried out the electron and focused ion beam fabrication

under the supervision of Q.B. and R.H., respectively. S.L. and J.H.E. provided the isotopically enriched BN. G.Á.-P. performed the analytical calculations and the numerical simulations with assistance from V.G. and supervision from A.Y.N. G.Á.-P. was responsible for data analysis and curation. P.A.-G., G.Á.-P., J.D., A.Y.N., V.G. and R.H. discussed and developed the interpretation of the results. P.A.-G. and A.Y.N. coordinated and supervised the work. G.Á.-P. and P.A.-G. wrote the original manuscript with input from J.D., A.Y.N., R.H., V.G., and J.M.-S. **Competing interests:** R.H. is cofounder of Neaspec GmbH, a company producing scattering-type near-field scanning optical microscope systems, such as the one used in this study. The authors declare that they have no other competing interests. **Data and materials availability:** All data needed to evaluate the conclusions in the paper are present in the paper and/or the Supplementary Materials.

Submitted 1 March 2022

Accepted 7 June 2022

Published 20 July 2022

10.1126/sciadv.abp8486

Negative reflection of nanoscale-confined polaritons in a low-loss natural medium

Gonzalo Álvarez-PérezJiahua DuanJavier Taboada-GutiérrezQingdong OuElizaveta NikulinaSong LiuJames H. EdgarQiaoliang BaoVincenzo GianniniRainer HillenbrandJavier Martín-SánchezAlexey Yu NikitinPablo Alonso-González

Sci. Adv., 8 (29), eabp8486. • DOI: 10.1126/sciadv.abp8486

View the article online

<https://www.science.org/doi/10.1126/sciadv.abp8486>

Permissions

<https://www.science.org/help/reprints-and-permissions>

Use of this article is subject to the [Terms of service](#)

Science Advances (ISSN) is published by the American Association for the Advancement of Science. 1200 New York Avenue NW, Washington, DC 20005. The title *Science Advances* is a registered trademark of AAAS. Copyright © 2022 The Authors, some rights reserved; exclusive licensee American Association for the Advancement of Science. No claim to original U.S. Government Works. Distributed under a Creative Commons Attribution NonCommercial License 4.0 (CC BY-NC).